Ultraviolet photodissociation of HCl in selected rovibrational states: Experiment and theory

Paul M. Regan,[a] Daniela Ascenzi, Alex Brown,[b] Gabriel G. Balint-Kurti,
and Andrew J. Orr-Ewing[c]
School of Chemistry, University of Bristol, Bristol, BS8 1TS, United Kingdom

Experimental and theoretical methods have been applied to investigate the effect of internal parent excitation on the ultraviolet photodissociation dynamics of HCl ($X\,^1\Sigma^+$) molecules. Jet-cooled $H^{35}Cl$ molecules within a time-of-flight mass spectrometer were prepared by infra-red absorption in the following quantum states: $v=1$, $J=0$ and $J=5$; $v=2$, $J=0$ and $J=11$; $v=3$, $J=0$ and $J=7$. The excited molecules were then photodissociated at $\lambda\sim235$ nm and the Cl(^2P_j) photofragments detected using $(2+1)$ resonance enhanced multiphoton ionization. The results are presented as the fraction of total chlorine yield formed in the spin–orbit excited state, Cl($^2P_{1/2}$). The experimental measurements are compared with the theoretical predictions from a time-dependent, quantum dynamical treatment of the photodissociation dynamics of HCl ($v=1-3$, $J=0$). These calculations involved wavepacket propagation using the *ab initio* potential energy curves and coupling elements previously reported by Alexander, Pouilly, and Duhoo [J. Chem. Phys. **99**, 1752 (1993)]. The experimental results and theoretical predictions share a common qualitative trend, although quantitative agreement occurs only for HCl ($v=2$). © *2000 American Institute of Physics.* [S0021-9606(00)00923-5]

I. INTRODUCTION

The influences of vibrational and rotational excitations on molecular photodissociation dynamics have chiefly been considered for polyatomic molecules.[1] These vibrationally-mediated photodissociation (VMP) investigations traditionally identified the effect of the initial state preparation on the relative yields of product channels. For polyatomic molecules there is the possibility of forming a variety of chemical species in a wide range of asymptotic states, yet the dissociation of diatomic molecules occurs to just a handful of atomic quantum levels. This simplicity presents an attractive opportunity for rigorous, quantum mechanical calculations of the photodissociation dynamics to be compared with detailed experimental measurements. Laboratory studies of the VMP of diatomic molecules are, however, relatively sparse.[2,3]

Theoretical predictions of the effect of parent vibration on the branching between halogen spin–orbit states have been reported for HCl,[4,5] HBr,[6] and HI[7] molecules In all cases, the product branching as a function of excitation wavelength displayed an oscillatory behavior that reflected the nodal pattern of the initial vibrational wavefunction, although both studies of HCl computed particularly sharp variations in the branching yield over localized energy regions.

Numerous papers have been presented on the photodissociation of hydrogen halides in $v=0$ and successful progress has recently been achieved in addressing the photophysics of HCl ($v=0$). Quantitative agreement has been reported between the results of several experiments[8–10] and a high-level, time-independent quantum dynamics computation involving *ab initio* electronic states and coupling terms.[8] The same theoretical treatment was also applied to DCl[8] and the predictions were found to be in good agreement with recent measurements from our laboratory.[11]

The experimental results contained in this paper offer additional tests of the existing theoretical framework of the HCl system, which is further explored using a time-dependent treatment of the photolysis process. Specifically, HCl ($X\,^1\Sigma^+$) molecules were photodissociated following preparation in selected rotational states of vibrational levels $v=1-3$. The nascent Cl($^2P_{3/2}$) and Cl($^2P_{1/2}$) photofragments were detected by $(2+1)$ resonance enhanced multiphoton ionization (REMPI) that, with the use of a calibration factor, enabled a quantification of the branching between the product channels. These state-specific experimental determinations are compared with the results of wavepacket calculations of the dissociation dynamics using available *ab initio* electronic energies and coupling elements.[12,13]

II. EXPERIMENT

The experimental method employed was as follows: a sample of HCl was excited to a particular rovibrational level of the ground electronic state using tunable infrared (IR) laser radiation. A second laser beam, of ultraviolet (UV) light, subsequently photolyzed the prepared HCl (v,J) molecules and state-selectively ionized the Cl(^2P_j) photofragments. The production of Cl$^+$ ions was monitored using a Wiley–McLaren configured time-of-flight (TOF) mass spectrometer

[a]Current address: Chemical Sciences Division, Ernest Orlando Lawrence Berkeley National Laboratory, Berkeley, California 94720.
[b]Current address: Department of Physics and Astronomy, University of Alabama, Box 870324, Tuscaloosa, Alabama 35487-0324.
[c]Author for correspondence. Telephone: +44 117 928 7672; fax: +44 117 925 0612; electronic mail: a.orr-ewing@bristol.ac.uk

(MS) as the UV wavelength was scanned over the full Cl-atom spectral feature. A detailed description of the apparatus is available elsewhere[14] and only details pertinent to this work will be recounted.

The IR radiation was generated in two ways. Wavelengths required for the first and second overtone bands of HCl were directly provided by the idler output of a commercial Nd:YAG pumped optical parametric oscillator (OPO) system (Spectra Physics, MOPO-730). Typical idler beam energies were ~4 mJ for the (2,0) band at $\lambda \sim 1.72-1.77$ μm and ~5 mJ for the (3,0) band at $\lambda \sim 1.18-1.20$ μm, with a pulse duration of ~5 ns. The nonlinear medium (β-barium borate, BBO) of the OPO unit does not, however, produce wavelengths corresponding to the fundamental vibrational band at $\lambda \sim 3.49-3.35$ μm. These wavelengths were obtained by difference-frequency mixing in a crystal (5 mm×5 mm×10 mm) of potassium titanyl phosphate (KTP), which is an efficient source of mid IR radiation when pumped by 532 nm light and seeded with $\lambda \sim 630$ nm.[15] The appropriate wavelengths for mixing were provided by a single Nd:YAG-dye laser system. Part of the second harmonic output of the Nd:YAG laser was separated using a beam splitter (nominally 60% reflective) and sent along a delay line to the KTP crystal. The transmitted 532 nm radiation pumped a dye laser (Sirah, Cobra-Stretch) to generate tunable, red light (at 627 $< \lambda <$ 633 nm) that was directed into the KTP crystal. A 532 nm dichroic mirror was used to merge the beams onto a colinear path through the mixing crystal. The IR beam was isolated from the visible elements using a barium fluoride Pellin–Broca prism and optical components composed of calcium fluoride were used on the subsequent path to the vacuum chamber. About 0.3 mJ of IR radiation was typically generated by this method. In all cases, an optoacoustic cell was used to locate the desired IR transition, which selectively excited just one of the two isotopomers of HCl. These were not expected to have significantly different photodissociation dynamics because the change in the reduced mass is so slight and so for the simple reason of a greater abundance, measurements were obtained for H^{35}Cl rather than for H^{37}Cl.

The HCl sample was introduced into the evacuated TOF MS by supersonically expanding through a pulsed nozzle a mixture of HCl and a rare gas. Several compositions, all at sub-atmospheric pressures, were used: 1% HCl in He; 10% HCl in Ar; and 20% HCl in Ar. No variation of the results with different gas mixtures was noted. The molecular beam was intersected at the center of the MS extraction region by focused ($f=50$ cm) IR light and after a typical time delay of 50 ns by a counterpropagating, UV laser pulse that both photodissociated HCl molecules and ionized the Cl atom products. The UV radiation was loosely focused ($f=50$ cm) and tuned accordingly for (2+1) REMPI of a particular spin–orbit state of Cl. The two-photon resonances of the REMPI schemes were $4p\,^2D_{3/2} \leftarrow 3p\,^2P_{3/2}$ (235.336 nm) and $4p\,^2P_{1/2} \leftarrow 3p\,^2P_{1/2}$ (235.205 nm).[16] The appropriate wavelengths were generated by frequency doubling in a BBO crystal the fundamental output of a dye laser (operating on Coumarin 460 dye) pumped by an Nd:YAG laser (this laser radiation is referred to later as the ''probe''). The UV pulse intensity was recorded by a photodiode viewing the fluores-

cence (in a cuvette containing a dilute dye solution) induced by a reflection of the main UV beam. Measurements using a power meter indicated routine UV energies of 0.3–0.5 mJ/pulse (in a ~5 ns pulse). The intensity of the IR pulse was monitored by directing a reflection of the main beam into a screened, IR-sensitive photodiode.

Chlorine ions were detected at the end of the TOF region by a pair of micro-channel plates coupled to a digital oscilloscope, which also registered the photodiode signal of the UV laser. Both of these signals (REMPI and diode) and the boxcar integrator output were downloaded to a personal computer and recorded after every laser shot as the UV laser wavelength was scanned slowly across the full linewidth of the REMPI transition. In principle, the Cl$^+$ signal could have been produced by the UV laser alone by photolysis of HCl ($v=0$) but the absorption cross-section is so small at $\lambda \sim 235$ nm that this contribution was always negligible; conditions were arranged such that the observed ion signal disappeared if either of the laser beams was blocked. As in our previous REMPI studies,[11,17] a data set consisted of consecutive scans over the Cl, Cl*, and Cl REMPI transitions (or vice versa) in order to highlight, and account for, long-term drifts in the experimental conditions.

III. THEORY

To aid in the interpretation of the experimental results, we performed grid-based time-dependent wavepacket calculations of the photodissociation dynamics using the electronic potential energy curves, transition dipole moments, and spin–orbit couplings reported by Alexander *et al.*[12,13] The time-dependent treatment of the photodissociation dynamics is based on the solution of the time-dependent Schrödinger equation:

$$i\hbar \frac{\partial}{\partial t} \Phi(R,t) = \hat{H}(R)\Phi(R,t), \tag{1}$$

where the time-independent Hamiltonian, $\hat{H}(R)$, is the sum of the radial nuclear kinetic energy operator (which includes the rotational Hamiltonian), the electronic potential energy, and the spin–orbit Hamiltonian:

$$\hat{H} = -\frac{\hbar^2}{2\mu} \frac{d^2}{dR^2} + \frac{\hbar^2}{2\mu R^2} \hat{l}^2 + V(R) + \hat{H}_{\text{so}}(R)$$

$$= \hat{T}(R) + V(R) + \hat{H}_{\text{so}}(R), \tag{2}$$

where R represents the position of one atom relative to the other. The effect of rotation on the photodissociation dynamics was shown in previous time-independent calculations to be negligible for HCl[4,8,12,18] and HBr,[19] and the $\hat{l}^2$ term has consequently been neglected in the time-dependent calculations considered in this study. The total Hamiltonian was comprised of

$$V_{\text{tot}} = V(R) + \hat{H}_{\text{so}}(R), \tag{3}$$

and the nuclear kinetic energy operator. Within the time-dependent framework,[20–22] a wavepacket Φ is created on an

J. Chem. Phys., Vol. 112, No. 23, 15 June 2000

Photodissociation of HCl   10261

excited potential energy curve by multiplying the ground state nuclear wavefunction Ψ by the appropriate transition dipole moment function μ:

$$\Phi(R,t=0)=\mu(R)\Psi(R). \tag{4}$$

In this equation $\mu(R)$ is a single component of a spherical vector. The initial wavepackets for an n-state problem are explicitly given by

$$\begin{pmatrix} \Phi_1(R,t=0) \\ \Phi_2(R,t=0) \\ \vdots \\ \Phi_n(R,t=0) \end{pmatrix} = \begin{pmatrix} \mu_1(R)\Psi(R) \\ \mu_2(R)\Psi(R) \\ \vdots \\ \mu_n(R)\Psi(R) \end{pmatrix}, \tag{5}$$

where $\Phi_j(R,t)$ represents the wavepacket associated with the electronically excited state j and $\mu_j(R)$ is the transition dipole moment component connecting the ground electronic state with the excited state j.

The formal solution to Eq. (1) is

$$\Phi(t)=\exp(-i\hat{H}t/\hbar)\Phi(t=0), \tag{6}$$

where $\exp(-i\hat{H}t/\hbar)$ is the time-evolution operator, which is used in the time-dependent method to propagate the wavepackets Φ_j on the coupled, excited state surfaces in a series of short time steps. After each time step, the autocorrelation function, $A(t)$, is calculated:

$$A(t)=\sum_j \int_0^\infty \Phi_j^*(R,t=0)\Phi_j(R,t)dR. \tag{7}$$

The total cross-section as a function of the frequency of the incident radiation is given by the Fourier transform of the autocorrelation function as function of time.[20,21] The total integral cross-section in SI units may be calculated using the equation

$$\sigma^{\mathrm{tot}}(\nu)=\frac{\pi\nu}{3c\epsilon_0\hbar}\int_{-\infty}^\infty \exp[i(E_{\mathrm{ini}}+h\nu)t/\hbar]A(t)dt, \tag{8}$$

where E_{ini} is the energy of the initial state.

The partial cross-sections for the formation of particular dissociation product channels are obtained by examining the wavepacket associated with each of the excited electronic state surfaces at a large internuclear separation, $R=R_\infty$, in the asymptotic region where no further couplings between electronic states take place. It can be shown[23] that the partial cross-section for the jth channel is given by

$$\sigma_j(\nu)=\left(\frac{4\pi^3\nu k_j}{3c\epsilon_0 m}\right)|A_j(R_\infty,E)|^2, \tag{9}$$

where

$$A_j(R_\infty,E)=\frac{1}{2\pi}\int_0^\infty \Phi_j(R_\infty,t)\exp[i(E_{\mathrm{ini}}+h\nu)t/\hbar]dt, \tag{10}$$

and k_j is the wavevector of the photofragments and m is their reduced mass.

The numerical parameters used to perform the time-dependent wavepacket calculations are reported in Table I. The wavepackets must be damped out when they reach the asymptotic region of the grid, otherwise the periodic nature

TABLE I. Numerical parameters used to perform the time-dependent wavepacket calculations.

Range of grid/bohr	1.0 to 20.0
Number of grid points	1024
Number of time steps	4096
δt/fs	0.0241888
R_∞/bohr	12.0
R_{damp}/bohr	15.0
C_{damp}/hartree	0.3346

of the Fourier transforms causes a reappearance at the small R end of the grid. The asymptotic wavefunctions were damped accordingly using a cubic complex absorbing potential,[24] defined by

$$V_{\mathrm{damp}}(R)=0.0, \quad R<R_{\mathrm{damp}};$$

$$V_{\mathrm{damp}}(R)=-iC_{\mathrm{damp}}\left(\frac{R-R_{\mathrm{damp}}}{R_{\mathrm{max}}-R_{\mathrm{damp}}}\right)^3, \quad R_{\mathrm{damp}}<R<R_{\mathrm{max}}; \tag{11}$$

where R_{damp} is the point where the damping is switched on, and C_{damp} is an optimized parameter giving the strength of the damping.

The above discussion of the time-dependent treatment of photodissociation dynamics is entirely general. Two particular basis sets are convenient, however, when considering nonadiabatic processes: a diabatic or an adiabatic basis. The relationship between the two basis sets can be expressed as

$$\Phi^{\mathrm{ad}}(R)=\mathbf{M}(R)\Phi^{\mathrm{diab}}(R), \tag{12}$$

where $\mathbf{M}(R)$ is a unitary matrix that continuously diagonalizes the total potential energy term, $V_{\mathrm{tot}}(R)=V(R)+\hat{H}_{\mathrm{so}}(R)$, at each value of the internuclear separation. In the diabatic representation, the radial nuclear kinetic energy operator, $\hat{T}(R)$, and $V(R)$ are diagonal, and off-diagonal terms occur in $\hat{H}_{\mathrm{so}}(R)$. The adiabatic potential energy curves, $V^{\mathrm{ad}}(R)$, can be defined by

$$V^{\mathrm{ad}}(R)=\mathbf{M}(R)V_{\mathrm{tot}}(R)\mathbf{M}^T(R). \tag{13}$$

Twelve electronic molecular states result from the combination of the $H(^2S)+Cl(^2P)$ species but only the ground state, $^1\Sigma^+(0)$, and the four excited states that connect to the ground state via an electric dipole transition, $^3\Pi(1)$, $^1\Pi(1)$, $^3\Sigma^+(1)$ and $^3\Pi(0^+)$, are used in considering the photodissociation dynamics of HCl. The adiabatic, e-parity potential energy curves of these states are shown in Fig. 1. The term symbols translate as a mixed Hund's case (a)/case (c) according to $^{2S+1}\Lambda(\Omega)$; where Ω is the only good quantum number for Hund's case (c). The case (a) and case (c) labels correspond to the diabatic and adiabatic representations, respectively.

The initial wavepackets are created in the diabatic representation according to Eq. (5), which requires that μ and Ψ are created from diabatic basis functions. The $ab\ initio$ transition dipole moment for $^1\Pi\leftarrow{}^1\Sigma^+$ was directly provided in the diabatic basis, but the transition moment of $^3\Pi(0^+)\leftarrow{}^1\Sigma^+(0)$ must be computed in the adiabatic case (c) representation as it arises from spin–orbit coupling of the diabatic
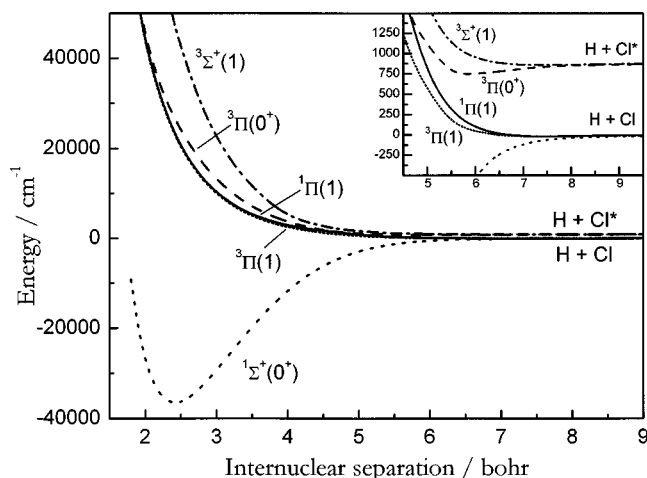
FIG. 1. Plot of the adiabatic potential energy curves of HCl used in the time-dependent calculations. The functions were generated using information from Ref. 12 and the correlations shown are appropriate for the *e*-parity components. The inset shows an expanded view of the long-range parts of the potentials. The different curves are: $X\,^1\Sigma^+(0^+)$ [- - -]; $^3\Pi(1)$ [· · · ·]; $^1\Pi(1)$ [—]; $^3\Pi(0^+)$ [- - -]; $^3\Sigma^+(1)$ [— · — · — · —].

$^1\Sigma^+$ state and the $\Omega=0^+$ component of the $^3\Pi$ state. As Ω is a good quantum number, the dynamical calculations for the evolution of the wavefunction can be broken up into two noninteracting parts: one for $\Omega=1$ and another for $\Omega=0$. The $\Omega=0$ part should in principle include two diabatic states corresponding to $^1\Sigma^+(0)$ and $^3\Pi(0^+)$. As the potential energy curves for these diabatic states are separated by a very large energy in the Franck–Condon region, we have not included this coupling in the dynamical calculations. The $^3\Pi(0^+)$ $\leftarrow {}^1\Sigma^+(0)$ transition dipole moment calculated using the adiabatic states is therefore used to create the initial wavepacket on the diabatic $^3\Pi(0^+)$ curve, and the subsequent dynamics are carried out on the diabatic $^3\Pi(0^+)$ curve only. This means that all flux initially promoted to this state will dissociate to give excited state chlorine atoms, $\mathrm{Cl}(^2P_{1/2})$. The spin orbit coupling between the $^1\Sigma^+(0)$ and $^3\Pi(0^+)$ states will have a more significant effect in the asymptotic region, where the potential energy curves approach more closely. Also, in principle, the rotational Hamiltonian couples the $\Omega=0^+$ and $\Omega=1$ states, and this coupling has also been neglected in the calculations. As a consequence of omission of these two effects, the contribution of the $^3\Pi(0^+)$ state to the production of excited state chlorine may be overestimated.

The initial wavepacket [Eq. (5)] given in the diabatic basis is

$$\Phi^{\mathrm{diab}}(R,t=0)=\begin{pmatrix} 0 \\ \mu_1(R)\Psi(R) \\ 0 \\ \mu_2(R)\Psi(R) \end{pmatrix}, \qquad (14)$$

where $\mu_1(R)$ is the $^1\Pi\leftarrow {}^1\Sigma^+$ transition moment and $\mu_2(R)$ is the $^3\Pi(0^+)\leftarrow {}^1\Sigma^+(0)$ transition moment. The ground vibrational state wavefunction $\Psi(R)$ was determined using the

Fourier grid Hamiltonian method.[25] The model assumes that in the diabatic, case (a) basis there is no photoexcitation to the $^3\Pi(1)$ or $^3\Sigma^+(1)$ states.
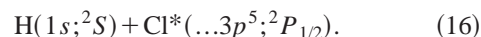
The Chebychev propagation scheme[26,27] was used to solve the time-dependent nuclear Schrödinger equation. The diabatic basis is considered here to be the primary basis, although all analysis of the wavepacket is performed in the adiabatic basis. When acting with the total Hamiltonian for a given time-step, the propagation requires (i) two transformations, $\mathbf{M}(R)$ and $\mathbf{M}^T(R)$, to change between the diabatic and adiabatic representations, see Eq. (12), and (ii) two fast Fourier transforms (FFTs) to switch between the coordinate and the momentum representations. These transformations simplify the calculation of different parts of the total Hamiltonian. An initial FFT expresses the diabatic wavepackets in the momentum representation where the action of the kinetic energy operator becomes a simple multiplication, rather than a complicated derivative.[22,27] An inverse FFT then returns the wavepackets to the diabatic, coordinate representation. The total potential energy term V_{tot} is diagonal in the adiabatic, coordinate basis and so the wavepackets are transformed to the adiabatic representation to operate with V_{tot}. The calculation for the time-step is completed with an adiabatic-to-diabatic transformation that gives a new set of wavepackets on the diabatic potential energy curves. At the end of the cycle, these diabatic wavepackets reflect the action of the Hamiltonian that can transfer flux between the electronic states. The wavepackets are analyzed using Eqs. (9) and (10) in the adiabatic representation. Although each propagation step required several manipulations to ensure the dynamics on the coupled potential energy curves was treated correctly, just one time-dependent computation yielded observables of interest, e.g., partial cross-sections, over a very wide range of energy.

The wavepacket calculations were tested by comparing results with those obtained for HCl ($v=0$) photolysis using time-independent methods.[8] With the methodology described above, the electronic potential energy curves, transition dipole moments, and spin–orbit couplings reported in Refs. 12 and 13, and the numerical parameters from Table I, the time-dependent calculations reproduced the results for the excited state spin–orbit branching fraction for HCl ($v=0$) photolysis as presented in Fig. 5 of Ref. 8.

IV. RESULTS AND DISCUSSION

A. Measured Cl* branching fractions

The experimental goal of this work was to characterize the branching between the spin–orbit states of the $\mathrm{Cl}(^2P)$ photofragments formed by photodissociating HCl in selected rovibrational states:

$$\mathrm{HCl}(v,J)+h\nu\rightarrow\mathrm{H}(1s;{}^2S)+\mathrm{Cl}(...3p^5;{}^2P_{3/2}), \qquad (15)$$

$$\mathrm{H}(1s;{}^2S)+\mathrm{Cl}^*(...3p^5;{}^2P_{1/2}). \qquad (16)$$

This result is conveniently expressed as the $\mathrm{Cl}(^2P_{1/2})$ branching fraction:

$$\Gamma=\frac{\sigma(\mathrm{Cl}^*)}{\sigma(\mathrm{Cl})+\sigma(\mathrm{Cl}^*)}, \qquad (17)$$

J. Chem. Phys., Vol. 112, No. 23, 15 June 2000
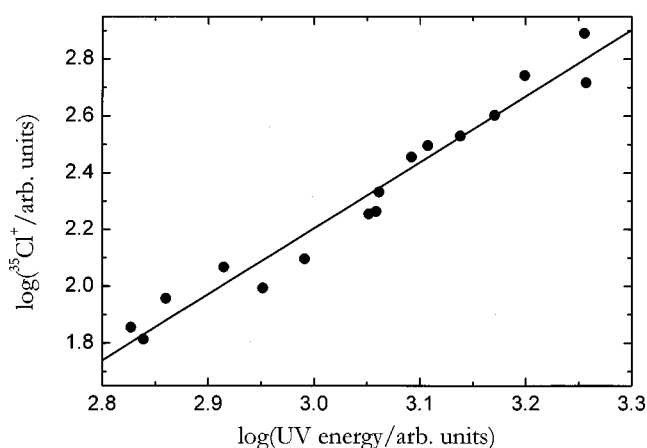
Photodissociation of HCl   10263

FIG. 2. Log–log plot of the integrated ^{35}Cl REMPI signal ($\bullet$) recorded at various probe pulse energies. The ion signal is assumed to scale with (probe energy)^m. A value for m of 2.3 was obtained from the gradient of a linear best-fit (solid line).

TABLE II. Measured ^{35}Cl($^2P_{1/2}$) branching fractions (see the text).

Prepared state: HCl (v,J)	IR transition	Equivalent 1-photon energy/cm^{-1} [a]	Γ [b] This work	Γ [c]
$v=1, J=0$	$P(1)$	45 444	0.51±0.05	0.44
$v=1, J=5$	$R(4)$	45 748	0.53±0.06	0.44
$v=2, J=0$	$P(1)$	48 226	0.44±0.07	0.45
$v=2, J=11$	$R(10)$	49 515	0.43±0.06	0.44
$v=3, J=0$	$P(1)$	50 905	0.40±0.06	0.43
$v=3, J=7$	$R(6)$	51 437	0.41±0.07	0.43

[a]Calculated as the energy of the rovibrational state (relative to $v=0$, $J=0$) plus the mean energy of the UV photons (42 506 cm^{-1}).
[b]Defined by Eq. (17). Errors correspond to 1σ.
[c]Theoretical prediction[8] of Γ for HCl ($v=0$) at the photolysis energy given in column 3.

where σ(Cl) and σ(Cl*) are, respectively, the cross-sections for the formation of Cl($^2P_{3/2}$) and Cl($^2P_{1/2}$) products.

To derive a value of Γ from the chlorine REMPI measurements it is necessary first to correct the signal for IR and UV intensity variations and then take into account the relative ionization efficiencies of Cl and Cl*. The REMPI signal was assumed to vary linearly with the IR energy and so was scaled directly to the IR-photodiode signal. The UV energy-dependence of the ion signal was investigated experimentally by recording the REMPI signal at different lamp-to-Q switch time delays of the ''probe'' Nd:YAG laser.

Figure 2 shows the results as a log–log plot of the ^{35}Cl REMPI signal against relative UV laser energy. The ion signal is assumed to scale with (probe energy)^m and a linear fit to the gradient of the log–log plot returned a best-fit value of $m=2.3$, which was the exponent used to normalize all REMPI data. In practice though, this correction had a minimal effect on the result as careful attention ensured uniform UV energies for, and across, each of the REMPI transitions. Once normalized, the REMPI signal was extracted by integrating the whole linewidth.

The subject of the relative ionization probabilities for common chlorine REMPI transitions was discussed in detail in Ref. 10, in which was presented an experimentally-determined scaling factor for the REMPI schemes. The same factor of 1.06 was used in this work to convert a ratio of normalized REMPI intensities of Cl*/Cl to a ratio of nascent populations of Cl*/Cl, which were then re-expressed as Γ.

Table II presents the spin–orbit branching fractions for the $\lambda\sim235$ nm photodissociation of HCl prepared in the following quantum states: $v=1, J=0$ and $J=5$; $v=2, J=0$ and $J=11$; $v=3, J=0$ and $J=7$. These states were chosen to compare the effects of rotation and vibration on the photodissociation dynamics. For each vibrational level, the highest rotational state was chosen that gave a sufficient signal that depended fully on both IR and UV beams. The factors of major influence were IR pulse energy, IR absorption cross-section, and molecular beam temperature. The combination of these elements gave rise to the wide variation of the

higher rotational states of each vibrational level.

The low pressure environment of the molecular beam and short time delay between IR and UV laser pulses limited the likelihood that rovibrational states other than the initially prepared one contribute to the photodissociation signal. A more reasonable concern was the effect of preparing a sample with aligned axes that can be created by the absorption of linearly polarized light. Preparation of the $v=1$, $J=5$ state by an $R(4)$ transition created the highest degree of alignment in this study; isotropic samples resulted from $P(1)$ transitions. For a diatomic molecule, a transition dipole moment lies either parallel or perpendicular to the internuclear axis and so an alignment of the parent axis distribution can be correlated to an alignment of transition dipole moments. This initial condition could bias a measurement of the product branching in cases—for example, HI—where different photolysis products arise from transition dipole moments of opposite symmetries. (While scanning over the full REMPI line effectively samples all recoil velocities and averages out any directional preference of the photolysis process, it does not compensate for the effect on the photodissociation yield caused by the parent molecule alignment.) For HCl, however, the evidence from experimental studies of $v=0$ molecules indicates that both dissociation channels arise predominantly from a perpendicular absorption.[9,10] A significant departure from this behavior was not expected for higher vibrational levels. It is thus concluded that the reported branching fractions are accurate measurements of the photodissociation of the initially prepared rovibrational states.

For comparison with the present results (summarized in Table II), Lambert et al.[8] measured $\Gamma=0.33(\pm0.05)$ for photolysis of a molecular beam sample of HCl at $\lambda=235.3$ nm (the photolysis wavelength used herein), in excellent accord with the accompanying results from the high-level, quantum dynamics simulation. All values of Γ presented in Table II are higher than 0.33, signifying a change in the photodissociation dynamics from $v=0$. Curiously, a strikingly good agreement between the experimental results for $v=2$ and $v=3$ and the theoretical predictions for $v=0$ is observed if the total energy of the system (i.e. the energy of the rovibrational state plus the UV photolysis energy) is considered. The relevant values are given for inspection in the last column of Table II.
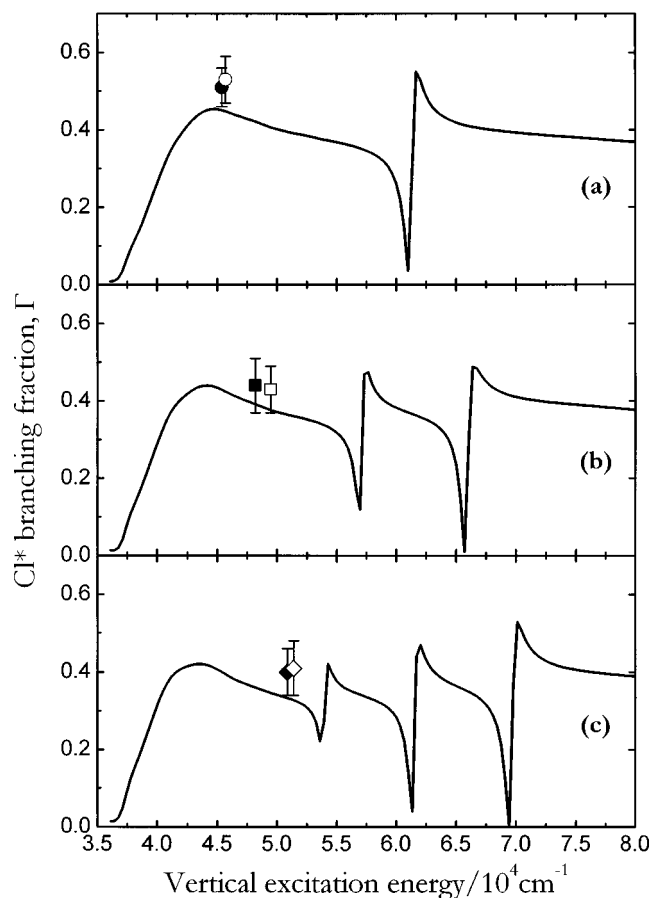
FIG. 3. A plot of the calculated Cl* branching fractions as a function of excitation energy for the photodissociation of HCl ($X\,^1\Sigma^+,v$) in (a) $v=1$; (b) $v=2$; (c) $v=3$. The solid lines apply to the wavepacket results for $J=0$ using the potential energies, coupling elements, and transition dipole moments of Refs. 12 and 13. The abscissa is the energy equivalent to a 1-photon excitation from $v=0$, $J=0$. Also shown are the Cl REMPI measurements presented in Table II: $v=1$, $J=0$ (●); $v=1$, $J=5$ (○); $v=2$, $J=0$ (■); $v=2$, $J=11$ (□); $v=3$, $J=0$ (◆); $v=3$, $J=7$ (◇). Note that the experimental data all lie on the low energy side of the HCl absorption band and experiments at higher photon energies are desirable as further tests of the calculations.

The data in Table II provide direct, experimental evidence that parent rotation has a negligible influence on the UV photodissociation dynamics of HCl. Former theoretical studies[12,18] of HCl examined the role of rotational couplings on the photodissociation dynamics and predicted no significant effect. The results herein, especially Γ for $v=2$, $J=0$ and 11, convincingly corroborate these previous assessments and justify the neglect of $\hat{H}_{\mathrm{rot}}$ from the Hamiltonian used in the theoretical calculations.

B. Time-dependent wavepacket calculations

The central results from the time-dependent wavepacket computations of this paper are the predicted excitation-energy dependences of Γ for initial HCl vibrational levels of $v=1$, 2, and 3, for $J=0$ in all cases. These values are derived by putting the calculated partial cross-sections from Eq. (9) into Eq. (17). These results are depicted in Fig. 3, which also includes the corresponding experimental results. In the following paragraphs, the calculated values of Γ are

first compared with the chlorine REMPI measurements and then discussed along with other findings from the theoretical investigation that shed light on the photodissociation mechanism of HCl.

The theoretical results are, overall, in good accord with the experimental observations: the broad trend of lower values of Γ for higher vibrational levels is correctly predicted by theory, although there seems to be a small, global underestimation of the branching fraction from the theoretical calculations. Alternatively, a question may be raised about the accuracy of the scaling factor used to extract the spin–orbit branching fractions from the observed REMPI signals. The pair of chlorine REMPI transitions employed herein were also employed by Lambert *et al.*[8] who used a scaling factor of 1.15.[28] Application of this value to the current data, however, leads to a greater difference between the experimental values and the calculations. Moreover, a revision of the scaling factor would have repercussions for the previously observed agreement between the experimental and theoretical branching fractions for DCl.[11]

In the calculation of the photodissociation dynamics, the production of Cl* stemmed from transitions from the $^1\Sigma^+$ ground state to the $^1\Pi$ and $^3\Pi(0^+)$ excited states [Eq. (14)]. The absence of rotational coupling in the calculation means that the dissociation dynamics subsequent to these excitations can be considered separately and these are the subjects of the following paragraphs.

1. Transition dipole moment between $\Omega=0$ states

The wavepacket created on the $^3\Pi(0^+)$ potential energy curve propagated solely on this excited state and so the yield of Cl* could be arbitrarily enhanced by increasing the magnitude of the $^3\Pi(0^+)\leftarrow{}^1\Sigma^+(0)$ transition dipole moment. Test calculations revealed that no simple increase of this transition moment would bring the theory into better agreement with the experimental data. Absorption to the $^3\Pi(0^+)$ potential energy curve is most significant at low energies ($\sim$40 000 cm^{-1}) and makes a negligible contribution towards Γ at energies at and above 50 000 cm^{-1}, i.e., around the energy of the $v=3$ experimental data. This analysis assumed that the functional form of the $^3\Pi(0^+)\leftarrow{}^1\Sigma^+(0)$ transition moment was accurate and that only the magnitude was in need of revision. This may not, of course, be true, but such an improvement would require improved electronic structure calculations. A clearer identification of inaccuracies of the $^3\Pi(0^+)\leftarrow{}^1\Sigma^+(0)$ transition dipole moment function could be supplied experimentally by further determinations of Γ at low excitation energies and by measurements of the angular anisotropy parameter of channel (16).

2. Nonadiabatic transitions during dissociation

As an alternative to dissociation via the $^3\Pi(0^+)$ state, a rise in Γ may be looked for in the mechanism of Cl* production following the (diabatic) $^1\Pi\leftarrow{}^1\Sigma^+$ transition. As commented above, diabatic and adiabatic models are useful when discussing photodissociation dynamics. Adiabatic potential energy curves are particularly appealing for treating the break-up of HCl because the correct spin–orbit product channels are attained at long range, although the diabatic
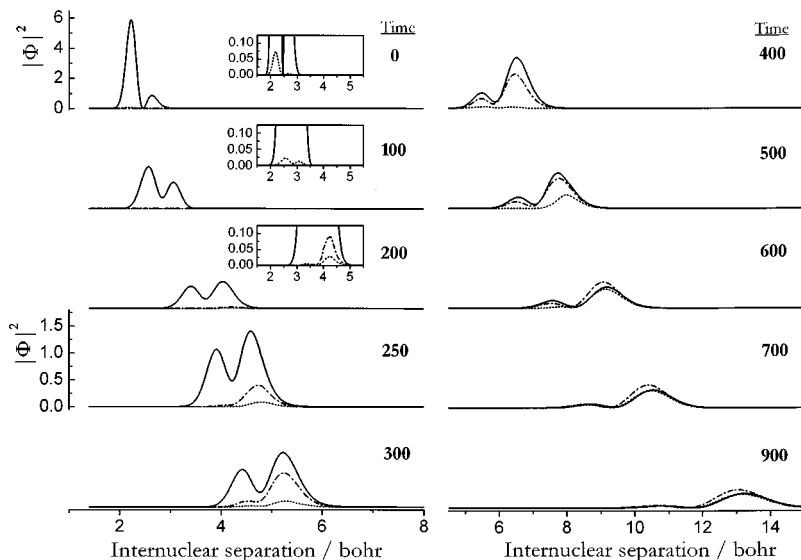
FIG. 4. Adiabatic wavepackets plotted for various time steps from $t=0$ to $t=900$ for the photodissociation of HCl ($v=1$). Each adiabat is identified by the diabatic component that is dominant in the Franck–Condon region: $^3\Pi(1)$ [· · · ·]; $^1\Pi(1)$ [——]; $^3\Sigma^+(1)$ [— · — · — · —]. All wavepackets are plotted on the same arbitrary scale. The wavepackets for $t\leqslant 200$ should be referred to the ordinate axis shown at $t=0$ and the wavepackets for $t\geqslant 250$ to the expanded axis at $t=250$. The insets show expanded regions to make clear the contribution at early time from the $^3\Pi(1)$ state in the FC region. One time step equals 0.024 fs.

representation can be more useful for identifying the onset of physical interactions. Figure 4 shows the evolution of wavepackets on the $^3\Pi(1)$, $^1\Pi(1)$, and $^3\Sigma^+(1)$ adiabatic potential energy curves following creation from the $v=1$ level of HCl. An equivalent plot for DCl is shown for comparison in Fig. 5. The wavepackets are shown at various time step intervals (1 time step equals 0.024 fs) from $t=0$ to $t=900$, by which time the dissociation is effectively complete. The squared amplitudes ($|\Phi|^2$) of the wavepackets are plotted on the same arbitrary scale throughout but the vertical axis is expanded for the plots of $t\geqslant 250$ for HCl and of $t\geqslant 350$ for DCl. Each wavepacket is associated with an adiabatic potential energy curve and is distinguished by the diabatic, case (a) state that makes the largest contribution to the adiabatic potential energy curve in the molecular region. It is important to appreciate that the wavepackets reflect the photodissociation dynamics over an energy range of about 100 000 cm^{-1}. The plots for $t=0$ reveal the dominance of the $^1\Pi(1)\leftarrow{}^1\Sigma^+(0)$ transition in the overall absorption, although a weak excitation of the $^3\Pi(1)$ state is also present as highlighted in the insets. This indicates that the spin–orbit

mixing within the $\Omega=1$ manifold of states of $^3\Pi$, $^1\Pi$, and $^3\Sigma^+$ within the FC region is not significant, which is reasonable because the diabatic potential energy curves have large energy differences compared with the spin–orbit splitting. The plots of subsequent time steps illustrate that the first dynamically significant event is a rapid, substantial transfer of flux from the $^1\Pi(1)$ state to the $^3\Sigma^+(1)$ state that begins at an internuclear separation of approximately 4 bohr for both HCl and DCl (compare the $t=200$, 250, and 300 panels of Fig. 4 and the $t=300$, 350 and 400 plots of Fig. 5). When the bond extends to about 6–8 bohr, the wavepacket associated with the $^3\Pi(1)$ adiabat increases sharply, as seen by comparing the plots for $t=400$ and 500 for HCl and for $t=600$ and 700 for DCl. A concomitant decrease in the wavepacket on the $^1\Pi(1)$ curve occurs. At $t=900$, the $^3\Sigma^+(1)$ wavepacket is the major component for HCl, whereas the three $\Omega=1$ wavepackets of DCl have comparable weight. To simplify the discussion, the dissociation dynamics are considered in two parts: a strong coupling between the $^1\Pi(1)$ and $^3\Sigma^+(1)$ states at $R\sim 4$ bohr, and a longer range transfer
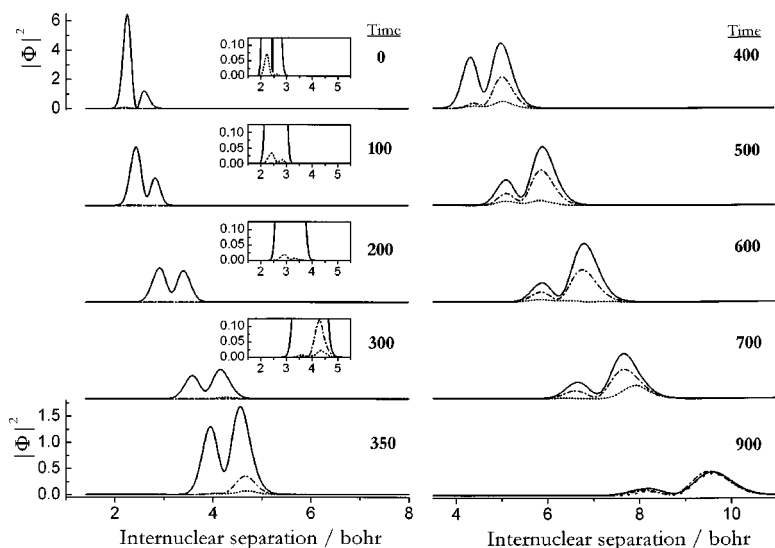

FIG. 5. An analogous plot to Fig. 4 for DCl ($v=1$) with adjusted x axes to compensate for the lower recoil velocity of the wavepacket. Note also that the axis is expanded in plots of $t\geqslant 350$ compared with the plots for $t\leqslant 300$. The wavepackets for DCl are plotted on the same scale as for HCl and can be compared accordingly.
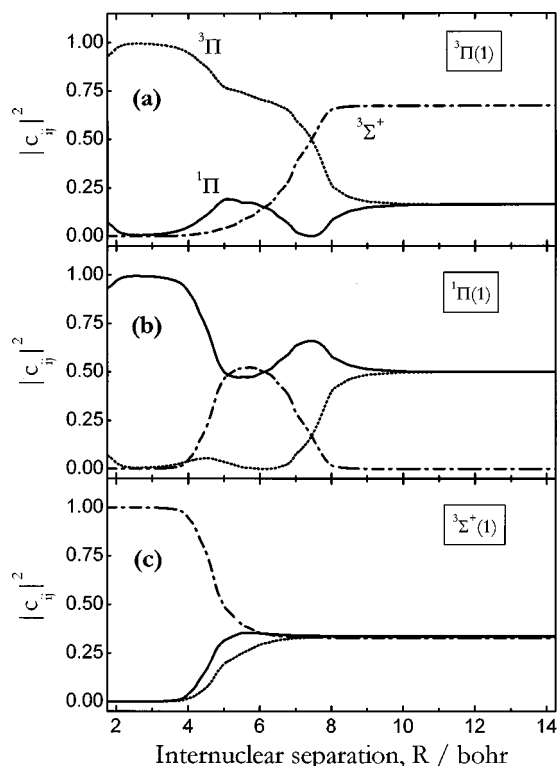
FIG. 6. Plot of the contributions $|c_{ij}|^2$, as a function of internuclear separation, of the $(\Omega=1)$ diabatic states $^3\Pi$ [· · · ·], $^1\Pi$, [——], and $^3\Sigma^+$ [—·—·—·—] towards the following adiabatic states of HCl: (a) $^3\Pi(1)$; (b) $^1\Pi(1)$; (c) $^3\Sigma^+(1)$.

of flux from the $^1\Pi(1)$ state to the $^3\Pi(1)$ potential energy curve.

Transitions between adiabatic states arise through terms of $\hat{T}_{\text{nuc}}$ that describe the derivative of the adiabatic electronic wavefunction with respect to the internuclear coordinate, i.e., how the make-up of the wavefunction changes from the molecular region to the asymptotic limits. This evolution can be examined by inspecting the unitary matrix $\mathbf{M}(R)$ that was used in the time-dependent calculations to switch between the adiabatic and diabatic representations. The elements of this matrix are the R-dependent coefficients that give the adiabatic states in terms of a linear combination of diabatic states [cf., Eq. (12)]:

$$\Psi_i^{\text{ad}}(R) = \sum_j c_{ij}(R)\Psi_j^{\text{diab}}(R). \qquad (18)$$

The contribution of a diabatic state Ψ_j^{diab} to the adiabatic state Ψ_i^{ad} is then obtained as $|c_{ij}|^2$. The contributions of the case (a), diabatic states $^3\Pi$, $^1\Pi$, and $^3\Sigma^+$, to the adiabatic states $^3\Pi(1)$, $^1\Pi(1)$, and $^3\Sigma^+(1)$ are given as functions of internuclear separation in Fig. 6. There is a sharp change at $R\sim 4$ bohr in the composition of the nominal $^1\Pi(1)$ state, which becomes a near 50:50 mixture of the $^3\Sigma^+$ and $^1\Pi$ states. A similar change is observed for the $^3\Sigma^+(1)$ state. This behavior results in the strong exchange of wavepacket flux between the $^1\Pi(1)$ and $^3\Sigma^+(1)$ adiabatic potential energy curves. A consideration of the diabatic representation of the electronic states reveals that the diabatic potential energy separations become comparable to the chlorine spin–orbit

splitting at about $R\sim 4$ bohr. Thus the strong change in the character of the adiabatic wavepackets may be identified with a region of angular momentum recoupling within the dissociating molecule.

The substantial interchange between the wavepackets on the $^1\Pi(1)$ and $^3\Sigma^+(1)$ potential energy curves is succeeded by a surge in the $^3\Pi(1)$ wavepacket that develops suddenly between $t=400$ and 500 for HCl and between $t=600$ and 700 for DCl, which places the onset of these nonadiabatic transitions to this state somewhere around 7–8 bohr. It appears from an inspection of the adiabatic wavepackets that the increased population of the $^3\Pi(1)$ potential energy curve occurs at the expense of the $^1\Pi(1)$ state. Figure 6 shows that there are significant changes in the diabatic state contributions of both the $^1\Pi(1)$ and $^3\Pi(1)$ adiabatic states between $R=7$ and 8 bohr. The potential energy curves at these long internuclear separations are almost at their asymptotic values and so this region of nonadiabatic coupling may be considered as the final angular momentum recoupling to form the correct atomic states of the asymptotic hydrogen and chlorine products.

These interpretations of the photodissociation dynamics following $^1\Pi\leftarrow{}^1\Sigma^+$ absorption do not lead to a simple diagnosis by which the theory may be modified in order to improve the agreement with the experimental results. The suggestions highlight, however, certain elements of importance, i.e., the precise form of the diabatic potential energies and couplings. Such influential factors in the dissociation process were further explored by investigating the detailed form of the excitation-energy dependence of Γ for the different initial vibrational levels.

3. Partial formation cross-sections for HCl and DCl

All the plots in Fig. 3 display broadly the same behavior observed previously[8] for the $v=0$ state, that is, a sharp increase in the relative production of Cl* as the energy increases from 35 000 to 45 000 cm^{-1}, and a tendency towards $\Gamma=1/3$ at higher energies. Superimposed onto this global pattern for the plot of each vibrational level are localized features where Γ oscillates rapidly within narrow energy ranges. These regions occur at approximately the same energies at which minima appear in the total absorption cross-section, which indicates that they may be understood as a reflection of the nodal structure of the ground electronic state vibrational wavefunctions. As mentioned earlier, these sharp oscillations of Γ over narrow energy ranges have been previously predicted for HCl.[4,5] Gersonde *et al.*[5] solved the time-dependent nuclear Schrödinger equation for excitation of HCl ($v=2$) on the excited potential energy curves of Givertz and Balint-Kurti[4] and of Alexander *et al.*[12] Both plots of the energy-dependence of the branching fraction displayed rapid oscillations in Γ at common energies, but there was a noticeable difference in the energy ordering of the maxima and minima in Γ: going from low to high energy, the results of Ref. 4 showed a maximum followed by a minimum, whereas the opposite trend was produced from the potential energy curves of Ref. 12. This comparison, using the same Hamiltonian but different potential energy functions for both data sets, strongly suggests that the relative energetic placements
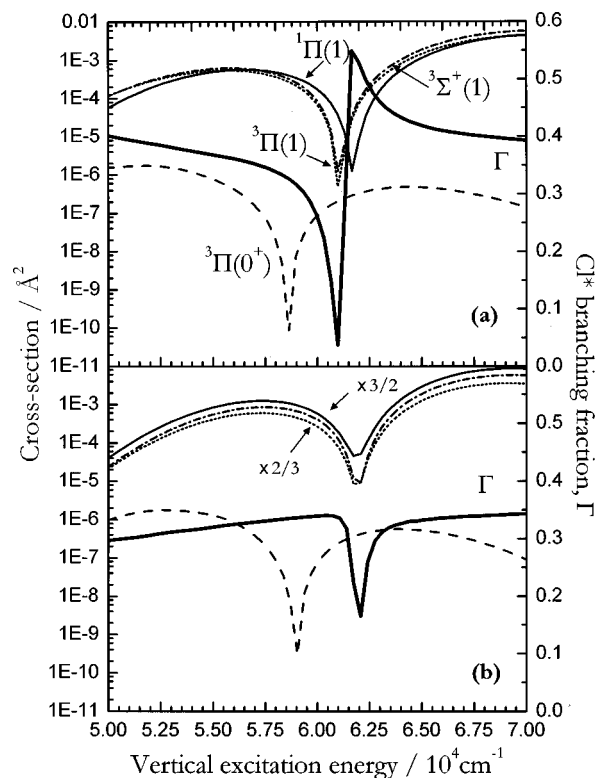
FIG. 7. Plot of the calculated partial cross-sections (left axis) for the photodissociation of (a) HCl ($v=1$, $J=0$) and (b) DCl ($v=1$, $J=0$): $^3\Pi(1)$ [· · · ·]; $^1\Pi(1)$ [———]; $^3\Sigma^+(1)$ [—·—·—·—]; $^3\Pi(0^+)$ [- - -]. Also shown is the relevant Cl* branching fraction (thick solid line), the value of which is given by the axis on the right. In (b), the values for the partial cross sections for the $^1\Pi(1)$ and $^3\Pi(1)$ states have, respectively, been multiplied and divided by 3/2 for presentation purposes in order to displace the curves vertically from that for the $^3\Sigma^+(1)$ state.

of the excited states are a dominant influence in determining the variation of Γ around the nodes, rather than details of the different coupling schemes used in Refs. 4 and 12. Thus, the experimental mapping of the branching fraction in the vicinity of the nodes would be a critical test of the potential energy curves.

The calculated spin–orbit branching fraction is directly derived from the partial cross-sections for the adiabatic potential energy curves and these are shown for HCl ($v=1$) in Fig. 7(a) for the regions around the sharp oscillation in Γ. It is seen that the partial cross-sections for the $^3\Pi(1)$ and $^3\Sigma^+(1)$ states have common minima at lower energy than for the cross-section of the $^1\Pi(1)$ state. The rapid variation of Γ in this region is a direct result of this splitting of the $\Omega=1$ partial cross-sections. The behavior of the spin–orbit branching fraction for photolysis of vibrationally-excited DCl differs somewhat from that observed for HCl. Figure 7(b) shows the energy dependence of Γ for photolysis of DCl ($v=1$) calculated from the partial cross-sections shown in the same plot. The variation of Γ around the nodal region is more moderate than displayed in Fig. 7(a) and the three $\Omega=1$ partial cross-sections have minima at about the same energy, in contrast with the HCl cross-sections.

The calculations reveal that the difference in energy between the minima of the $^3\Pi(0^+)$ and the $^1\Pi(1)$ cross-sections was the same for HCl ($v=1$) and DCl ($v=1$) and

was approximately equal to the difference between the $^3\Pi(0^+)$ and $^1\Pi(1)$ potential energy curves in the FC region. This supports the idea that each of these minima arises from a reflection of the ($v=1$) node onto the excited state potential energy curves. Speculation that the minima in the $^3\Pi(1)$ and $^3\Sigma^+(1)$ partial cross-sections occur for the same reason may be rejected because, in the FC region, the $^3\Pi(1)$ state lies at about the same energy as the $^3\Pi(0^+)$ and the $^3\Sigma^+(1)$ states is some 20 000 cm^{-1} higher than the $^1\Pi(1)$ state. In the preceding section we presented arguments for the formation of products on the $^3\Pi(1)$ and $^3\Sigma^+(1)$ adiabats by nonadiabatic transitions from the $^1\Pi(1)$ state. It is to be expected then that the nodal pattern in the initial wavepacket on the $^1\Pi(1)$ curve is carried into the wavepackets on the $^3\Pi(1)$ and $^3\Sigma^+(1)$ curves. Figure 7(a) demonstrates that the nodal structure manifests in the partial cross-sections for the $^3\Pi(1)$ and $^3\Sigma^+(1)$ states of HCl as minima that are energetically shifted from that for the $^1\Pi(1)$ adiabat. These off-sets are imposed by the nonadiabatic coupling that occurs during the fragmentation and, as the dissociation inherently involves several pathways, interference effects are possible. A more thorough investigation of this phenomenon has not proved tractable because the wavepacket propagation code necessarily covers a very broad energy range, while further exploration of these features requires the study of the wavepacket dynamics within a narrow energy spread.

V. CONCLUSIONS

Detailed experimental measurements of Γ for vibrationally-excited HCl have been compared with the results from wavepacket propagations on the best available *ab initio* potential energy curves, with due allowance for nonadiabatic dynamics. While the general agreement is good, the experimental measurements of Γ for vibrationally-excited HCl suggest slight inadequacies of the current electronic structure calculations of HCl, despite the previous successes of comparison between experiments and theory for the photolysis of HCl ($v=0$) and DCl ($v=0$). Refined *ab initio* calculations of the potentials and couplings for several excited states of HCl have very recently been published[29] and might improve the agreement between our experiments and theoretical calculations of branching fractions. The results also illustrate that measurements of the relative product branching yields from the photolysis of vibrationally-excited molecules offer highly sensitive tests of the theoretical descriptions of the potential energy curves, couplings, and transition dipole moments. This goal is challenging, however, as the measurement of the rapid variation of the branching yield over a small energy range calls for high precision determinations. A more feasible practical goal may be simply the determination of the energies at which the nodes in Γ occur. The experimental measurements of branching fractions presented here are restricted to the low energy side of the first HCl absorption band and further measurements at higher photon energies would provide additional stringent tests of the theoretical models.

Regan *et al.*

[1] F. F. Crim, J. Phys. Chem. **100**, 12725 (1996).

[2] J. Zhang, C. W. Riehn, M. Dulligan, and C. Wittig, J. Chem. Phys. **104**, 7027 (1996).

[3] D. J. Leahy, D. L. Osborn, D. R. Cyr, and D. M. Neumark, J. Chem. Phys. **103**, 2495 (1995).

[4] S. C. Givertz and G. G. Balint-Kurti, J. Chem. Soc., Faraday Trans. 2 **82**, 1231 (1986).

[5] I. H. Gersonde, S. Hennig, and H. Gabriel, J. Chem. Phys. **101**, 9558 (1994).

[6] B. Pouilly and M. Monnerville, Chem. Phys. **238**, 437 (1998).

[7] C. Kalyanaraman and N. Sathyamurthy, Chem. Phys. Lett. **209**, 52 (1993).

[8] H. M. Lambert, P. J. Dagdigian, and M. H. Alexander, J. Chem. Phys. **108**, 4460 (1998).

[9] J. Zhang, M. Dulligan, and C. Wittig, J. Chem. Phys. **107**, 1403 (1997).

[10] P. M. Regan, S. R. Langford, D. Ascenzi, P. A. Cook, A. J. Orr-Ewing, and M. N. R. Ashfold, Phys. Chem. Chem. Phys. **14**, 3247 (1999).

[11] D. Ascenzi, P. M. Regan, and A. J. Orr-Ewing, Chem. Phys. Lett. **310**, 477 (1999).

[12] M. H. Alexander, B. Pouilly, and T. Duhoo, J. Chem. Phys. **99**, 1752 (1993) (see Ref. 51).

[13] The values of the potential energies and coupling elements, as well as a FORTRAN code to calculate these, can be found in the Hibridon 4.1 Code, available for public distribution at the website: www-mha.umd.edu/~mha/hibridon.

[14] R. A. Morgan, A. J. Orr-Ewing, D. Ascenzi, M. N. R. Ashfold, W. J. Buma, C. R. Scheper, and C. A. de Lange, J. Chem. Phys. **105**, 2141 (1996).

[15] S. A. Reid and Y. Tang, Appl. Opt. **35**, 1473 (1996).

[16] The given assignment is taken from C. E. Moore, *Atomic Energy Levels*, Vol. 1, NBS Circ. 35 (Natl. Bur. Stand., Washington D. C., 1971), but is reassigned in the NIST Atomic Spectra Database (http://physics.nist.gov/cgi-bin/AtData/main_asd). More information is given in note 1 of Ref. 11.

[17] P. M. Regan, D. Ascenzi, C. Clementi, M. N. R. Ashfold, and A. J. Orr-Ewing, Chem. Phys. Lett. **315**, 187 (1999).

[18] S. C. Givertz, Ph.D. thesis, University of Bristol, 1982.

[19] G. Péoux, M. Monnerville, T. Duhoo, and B. Pouilly, J. Chem. Phys. **107**, 70 (1997).

[20] E. J. Heller, J. Chem. Phys. **68**, 2066 (1978); **68**, 3891 (1978).

[21] E. J. Heller, Acc. Chem. Res. **14**, 368 (1981).

[22] G. G. Balint-Kurti, R. N. Dixon, and C. C. Marston, Int. Rev. Phys. Chem. **11**, 317 (1992).

[23] G. G. Balint-Kurti, R. N. Dixon, and C. C. Marston, J. Chem. Soc., Faraday Trans. **86**, 1741 (1990).

[24] Á Vibók and G. G. Balint-Kurti, J. Phys. Chem. **96**, 8712 (1992).

[25] C. C. Marston and G. G. Balint-Kurti, J. Chem. Phys. **91**, 3571 (1989).

[26] H. Tal-Ezer and R. Kosloff, J. Chem. Phys. **81**, 3967 (1984).

[27] R. Kosloff, J. Phys. Chem. **92**, 2087 (1988).

[28] P. J. Dagdigian, private communication of the REMPI scaling factor used in Ref. 8.

[29] Y. Li, O. Bludsky, G. Hirsch, and R. J. Buenker, J. Chem. Phys. **112**, 260 (2000).